Wireless Reading and Localization of Additively Manufactured Galinstan-Based Sensor Using a Polarimetric Millimeter-Wave Radar Imaging Technique

Dominique Henry, Ahmad El Sayed Ahmad, Ali Hadj Djilani, Patrick Pons, Hervé Aubert

Wireless Reading and Localization of Additively Manufactured Galinstan-Based Sensor Using a Polarimetric Millimeter-Wave Radar Imaging Technique

Dominique Henry, Ahmad El Sayed Ahmad, Ali Hadj Djilani, Patrick Pons, and Hervé Aubert

***Abstract*— A polarimetric millimeter-wave radar imaging technique is proposed to remotely detect, localize, and wirelessly read a novel additively manufactured passive sensor composed of a microfluidic channel filled with liquid metal Galinstan. Very high variation of the radar-cross section of the sensor to small variations of the level of Galinstan in the channel is obtained. Indeed, at the radar-to-sensor distance of 2.4 m, the measured radar echo level of the sensor varies by 4.5 dB when the level of Galinstan changes by 1 mm. This sensitivity is higher than those previously reported in the literature for wireless and passive sensors of the same class. Moreover, the localization technique of the sensor is successfully achieved for only three false detections on 75 measurements in cluttered environments from radar-to-sensor distances up to 15 m.**

***Index Terms*— Additive manufacturing, Galinstan, liquid metal, polarimetry, radar imagery, remote monitoring, selective laser sintering.**

I. Introduction

REMOTE interrogation of wireless sensors is sometimes challenging, especially in industrial applications or harsh environments where human intervention, wiring, and/or battery replacement are not possible. In such environments, the use of passive and chipless sensors (i.e., sensors without batteries and integrated circuits) may be a suitable solution. Such devices, designated as chipless radio frequency identification (RFID) sensors, are still a research topic of great interest with issues related to multisensing [1], bio-compatibility [2], data density [3], or field polarization [4]. The counterpart is that the range of the wireless interrogation may be too short for many applications: the maximal reader-to-sensor distance of interrogation is typically 1 m for chipless RFID sensors to comply with effective isotropic radiated power (EIRP) standards [5]. Moreover, the sensors often present both low measurement sensitivity and small full-scale (or dynamic) measurement range, depending on the targeted application. A solution to increase both the dynamic range and the reader-to-sensor distance is to use a frequency-modulated continuous-wave (FM-CW) radar with directive receiving and transmitting antennas [6]. A 3-D beamscanning method combined with a dedicated radar image processing was also recently proposed [7]. Because industrial and harsh environments are often very reflective for RF waves, the remote reading of wireless sensors may be altered by the electromagnetic clutter. For this reason, efforts have been recently undertaken to increase the signal-to-noise ratio (SNR) by designing depolarizing chipless sensors [8] and to reach reader-to-sensor separation distance of five decades of meters [9]. A multisensor remote-reading approach in an industrial environment was also proposed in [10] using chipless pressure sensors manufactured from clean room technological facilities. The main issue of such sensors was their low measurement dynamic range, as their operating frequency was found to be slightly outside the radar modulation bandwidth. Moreover, these sensors required the use of delay lines (coaxial cables) that may not be suitable for a cost-effective and flexible multisensing approach in many practical applications. In this context, a cost-effective pressure chipless sensor was fabricated from additive manufacturing technology and microfluidic technology [11]. However, as the liquid was water in the first reported prototype, the proposed technological solution is not suitable for wide-range temperature measurement, especially below 0 °C at atmospheric pressure.

It has been shown that many transmission line technologies are compatible with additive manufacturing, such as finite-ground coplanar waveguides [12], [13], [14], microstrip lines [15], [16], [17], or substrate-integrated waveguides [18], [19], [20]. For wireless applications, printed antennas are part of the sensor and printed metallic waveguides (such as rectangular waveguides) with additive manufacturing may be a suitable solution [21], [22], [23]. Indeed, metallic hollow waveguides do not require a low-loss dielectric substrate (excepting the air) and can feed easily 3-D printed metallic antennas [24], [25], [26]. For these reasons, the metallic hollow waveguide technology printed from selective laser sintering (SLS) technique was applied in [11] for 3-D printing of only part of the wireless sensor and not the entire structure (the two cross-polarized sensor antennas and delay lines were actually not 3-D printed).

Manuscript received 8 May 2023; revised 22 June 2023; accepted 26 June 2023. This work was supported in part by the French Research Agency (ANR) as part of the S2LAM Project. *(Corresponding author: Dominique Henry.)*

Dominique Henry, Ahmad El Sayed Ahmad, and Patrick Pons are with the MINC Team, Laboratory for Analysis and Architecture of Systems, National Center for Scientific Research (LAASCNRS), 31000 Toulouse, France (e-mail: dhenry@laas.fr; ppons@laas.fr).

Ali Hadj Djilani and Herve Aubert are with the MINC Team, Laboratory for Analysis and Architecture of Systems, National Center for Scientific Research (LAASCNRS), 31000 Toulouse, France, and also with the National Polytechnic Institut (INP) of Toulouse University, 31000 Toulouse, France (e-mail: haubert@laas.fr).

Color versions of one or more figures in this article are available at https://doi.org/10.1109/TMTT.2023.3294549.

Digital Object Identifier 10.1109/TMTT.2023.3294549

The work presented in this article is an extended version of the article presented at the International Microwave Symposium 2023 [27] with additional and novel results. As for the initial article, the SLS technique is applied in Section II to entirely fabricate the passive sensor composed of a microfluidic channel filled with liquid metal Galinstan. It has a thermal expansion coefficient of 11.5 $\times$ 10^{-5} K^{-1} [28] at room temperature and can be used for the remote sensing of temperature variation [29]. Moreover, works proposed in [30], [31], [32], and [33] show that Galinstan-based radio frequency devices and additive manufacturing are well compatible. In Section III, we investigate the wireless interrogation of the proposed additively manufactured Galinstan-based sensor. It is shown that the level of Galinstan in the sensor's channel can be accurately estimated from the processing of isolines in polarimetric millimeter-wave radar images. Moreover, the proposed extended version of [27] includes novel results. The uncertainty and the precision of the measurement are estimated in Section III-C for different estimators. To demonstrate the feasibility of the remote reading of the sensor in industrial environments, various indoor scenarios are studied in Section III-D for different radar-to-sensor distances up to 15 m. In addition, an original algorithm, based on the processing of similar isolines in radar images, is applied in Section IV to localize the sensors in these scenarios and for different angles of interrogation.

II. Passive and Wireless Microfluidic Sensor

The combined use of Galinstan with an electromagnetic cavity is often motivated to design tunable devices such as bandpass filters [34], [35], [36], [37], [38], resonators [39], or phase-shifters [40], [41], [42]. In this work, the cavity acts as a temperature sensor. The proposed wireless and passive microfluidic sensor is a metallic waveguide structure composed of an electromagnetic cavity connected to two cross-polarized antennas. The electromagnetic cavity has a length of 9.2 mm delimited by two inductive irises. The schematic of the structure is displayed in Fig. 1(a). Dimensions of the cavity cross-section are those of a standard *WR28* rectangular waveguide (3.556 $\times$ 7.112 mm). A detailed view of the electromagnetic transducer is displayed in Fig. 1(b). One port of the cavity is connected to a vertically (V) polarized horn antenna. The second port of the cavity is connected to a horizontally (H) polarized horn antenna by using a bend (H-plane) rectangular waveguide followed by a 90° twisted rectangular waveguide. Such structure is designed to operate in the frequency bandwidth ranging from 22.8 to 24.8 GHz and its dimensions are 74.9 $\times$ 69.8 $\times$ 31.8 mm. The simulated gain of the two horn antennas at 23.8 GHz is 15.5 dBi and the half-power beamwidth is 25° in the E-plane and 31° in the H-plane. To be compliant with additive manufacturing technology, the two irises placed at the input and output of the cavity are triangular in shape. The cavity is crossed by a polytetrafluoroethylene (PTFE, relative permittivity of 2.1) microfluidic channel (internal diameter of 500 μm and external diameter of 800 μm) from two holes at the top and bottom of the metallic structure. Inside the channel flows the liquid metal Galinstan. The microfluidic channel crosses the cavity at its center, where the electric field of the fundamental resonant mode reaches its highest magnitude. A detailed view of the microfluidic channel with Galinstan through the waveguide is displayed in Fig. 1(c). The meniscus position l of Galinstan in the channel is called here "*the level of Galinstan*." When this level is 0 mm, it means that the microchannel placed inside the cavity is empty; when the level equals the height of the waveguide (i.e., when l = 3.556 mm), the channel inside the waveguide structure is completely filled with Galinstan.

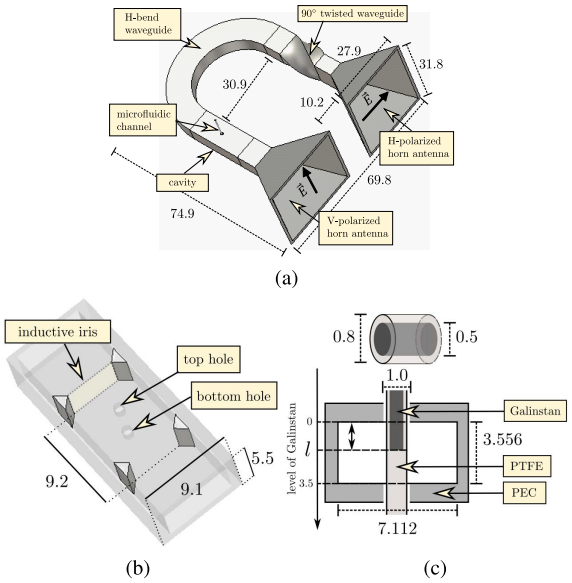

Fig. 1. (a) Three-dimensional schematic of the passive microfluidic sensor metallic structure. (b) Detailed view of the cavity. (c) Cross-sectional view of the microfluidic channel in the rectangular waveguide. Units are in mm.

In Fig. 2 (blue color), the simulated magnitude of the transmission coefficient S_{21} at 23.8 GHz of the two-port cavity is displayed as a function of the level of Galinstan (simulation results are obtained from the finite element method provided by the software Ansys HFSS). In this electromagnetic simulation, the Galinstan is modeled as a perfect electrical conductor (PEC). As expected, the decrease of the transmission coefficient $|S_{21}|$ is observed as the level of liquid metal in the channel increases. The (simulated) maximal dynamic range $\Delta|S_{21}|$ of 53 dB is obtained. It can be observed that the transmission coefficient continues to vary when the level l of metal liquid exceeds the height of the cavity (that is, when l > 3.556 mm). This variation is due to the excitation of the transverse electromagnetic (TEM) mode in the channel filled by the liquid: when the liquid crosses the wall of the cavity, the channel can be actually viewed as a small open-circuited coaxial transmission line.

Port 1 of the cavity is connected to the V-polarized horn antenna while port 2 is connected to the H-polarized horn antenna by using the H-bend rectangular waveguide followed by the 90° twisted rectangular waveguide. The simulated monostatic radar cross sections (RCSs) σ_{VV} and σ_{VH} of the structure are displayed in Fig. 3 as a function of the azimuth angle and for two levels of Galinstan: l = 0 and 3.6 mm. As the structure converts (due to its 90° twisted waveguide) the incident V-polarized field into a reradiated H-polarized field,

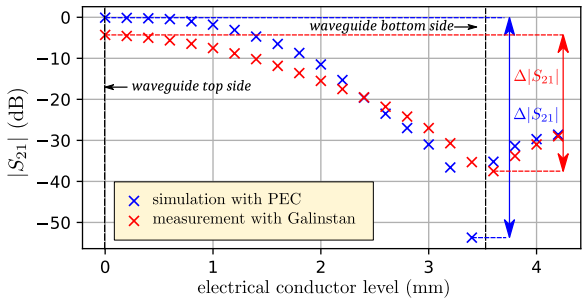

Fig. 2. Simulated (blue) and measured (red) transmission coefficient at 23.8 GHz as a function of the level of metal liquid in the channel (ohmic loss in the liquid metal is neglected in the electromagnetic simulation).

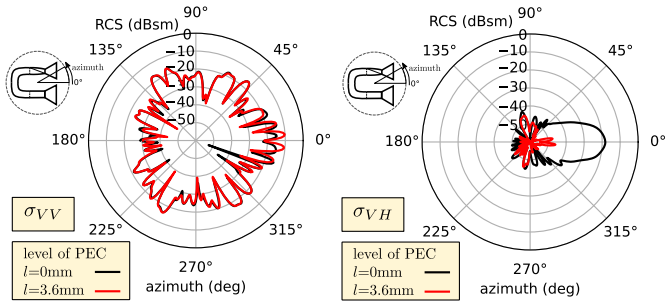

(a) (b)

Fig. 3. Simulated monostatic RCSs of the structure versus azimuth angle. (a) Co-polarized RCS σ_{VV}. (b) Cross-polarized RCS σ_{VH}. Black and red diagrams refer, respectively, to $l = 0$ mm (fluidic channel is empty) and $l = 3.6$ mm (channel is completely filled with metal liquid).

the (simulated) dynamic range offered by σ_{VH} (32 dB) is much higher than one achieved by σ_{VV} (5 dB).

The prototype of the microfluidic passive sensor is entirely fabricated from the SLS technique. The metal powder is stainless steel (316L with an electrical conductivity of 3×10^6 S/m and an average roughness of 7 μm). For practical reasons, the metallic structure is manufactured in five parts: the cavity, one single horn antenna, one horn antenna with the 90° twisted waveguide, and two sections of H-bend antenna. Flanges are added at waveguide terminations to assemble the different parts of the structure. The photograph of the resulting 3-D printed sensor is shown in Fig. 4(a).

The magnitude of the transmission coefficient S_{21} is measured by using a vector network analyzer for various levels of Galinstan. To control the level of Galinstan, the experimental setup shown in Fig. 4 is used. The cavity, crossed by the PTFE channel filled with Galinstan, is set on a micro-positioning table that performs translations with a displacement precision of few μm. The channel is static and both ends are sealed. The initial level of Galinstan is set with a microscope at the top edge of the metallic structure. Therefore, the level of Galinstan is 0 mm when the cavity is translated over the waveguide thickness (1.0 mm). When the micro-positioning table displaces the cavity along the channel, the level of Galinstan increases. We note that the uncertainty of the waveguide thickness is of ± 20 μm, and the curvature in the meniscus of the liquid metal induced an uncertainty of 10 μm on the level l of the Galinstan. Therefore, the level of Galinstan is estimated with a precision of ± 30 μm during the displacement of the cavity along the (static) channel. The measured magnitude of the

(a)

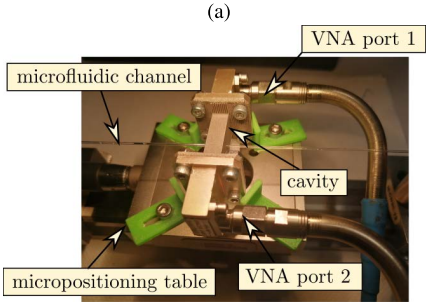

(b)

Fig. 4. (a) Micro-positioning table for the S-parameters measurement of the two-port cavity. (b) Photograph of additively manufactured 3-D structure (without the microfluidic part).

transmission coefficient as a function of the level of Galinstan is displayed in Fig. 2 (red color). The difference between the (lossless) simulation results and experimental data does not exceed 5 dB. We obtain a measured full dynamic range $\Delta|S_{21}| = 33$ dB, and consequently, a measured sensitivity $\Delta|S_{21}|/\Delta_l$ of 9.1 dB/mm. Between 0.8 and 3.0 mm, the sensitivity is slightly higher (9.3 dB/mm).

III. Polarimetric Radar Imaging of Passive and Wireless Microfluidic Sensor

A. First Scenario: Experimental Setup

In the first scenario, a 3-D beamscanning is performed using an FM-CW radar with carrier frequency f_c of 24.3 GHz and modulation bandwidth B of 2 GHz. As a result, the so-called theoretical depth resolution $d = c/(2B)$ (where c is the speed of light in vacuum) is found to be 7.5 cm. The radar front-end is composed of one transmitting channel (T_x) and two receiving (R_x) channels (model DK-sR-1030e from IMST GmbH [43]). The microwave power (20 dBm) transmitted by the radar through a lens-loaded vertically polarized (V-polarized) circular horn antenna (gain of 28 dBi and half-beamwidth of 6°). The receiving antennas are, respectively, V- and H-polarized rectangular horn antennas (gain of 20 dBi). At a distance of 2.4 m from the radar is located the depolarizing passive microfluidic sensor. The sensor operates in the frequency bandwidth of the radar, and its radar echo depends on the level l of Galinstan. The 3-D beamscanning is performed mechanically by using a pan-tilt that allows steering the main beam of the radar T_x-antenna with the azimuth (φ) sweep of $\pm 10°$ and angular speed $v_\varphi = 4°/s$. Since the chirps are transmitted with the repetition time $t_{rep} = 53$ ms, the azimuth angular step is $d_\varphi = v_\varphi \times t_{rep} = 0.2°$. The main beam sweep in elevation is $\pm 10°$ with the angular step of

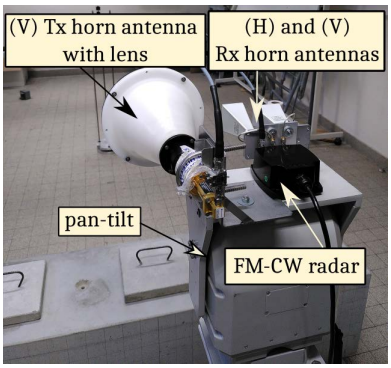

Fig. 5. Photograph of the 3-D beamscanning.

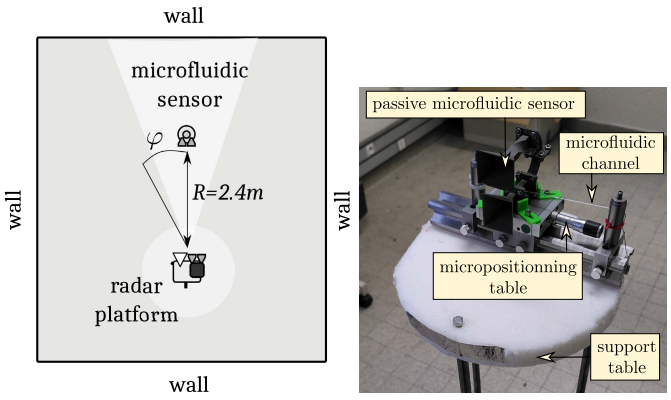

Fig. 6. (a) Illustration of scenario 1. (b) Photograph of the passive microfluidic sensor set on the micro-positioning table.

1°. A photograph of the radar mounted on the mechanical platform is shown in Fig. 5.

The microfluidic passive sensor is located in a room of our laboratory and placed at a distance of 2.4 m from the radar, as depicted in Fig. 6(a) and the sensor is set on a micro-positioning table in which the microfluidic channel filled with Galinstan is integrated. As previously indicated, the microfluidic channel crosses the metallic structure through the rectangular waveguide cavity [see Fig. 6(b)]. Beamscannings are performed for level l of Galinstan ranging from 0 to 4.6 mm through the channel with a step of 0.2 mm. In each direction (θ, φ) in space, the chirp is transmitted by the radar, and the beat frequency spectrum is obtained in this direction. Each spectrum is composed of $N_R = 256$ samples and the maximal radar interrogation distance $d_{\max}$ is then given by $d \times N_R$. The resulting 3-D image after a beamscanning is a matrix of size $N_\theta \times N_\varphi \times N_s$, where $N_\theta = 21$ and $N_\varphi = 105$ are, respectively, the number of samples in elevation and azimuth angles. Moreover, the radar images are obtained from four configurations of polarizations p that are defined by the polarizations of the transmitting and receiving antennas. Indeed $p =$ VV (or VH) if the measurement is performed by using a V-polarized transmitting antenna and a V- (or H-)polarized receiving antenna; equivalently, if the experiment is performed by using H-polarized transmitting antenna and V- (or H-)polarized receiving antenna, then $p =$ HV (or $p =$ HH).

B. Wireless Reading From Polarimetric Radar Imaging Technique in the First Scenario

The polarimetric radar images provided by the four configurations $p =$ VV, VH, HV, and HH at the radar-to-sensor distance of 2.4 m are displayed in Fig. 7 for levels of Galinstan inside the channel of 7(a) 0.0 mm and 7(b) 3.0 mm. Blue to yellow colors represent low (−30 dB) to high echo levels (10 dB). As expected from the design of the passive sensor, the radar echo level depends on the level of Galinstan in the channel, and high echo variation is obtained from the cross-polarized configurations VH and HV. To characterize the variation of echo level when the level of Galinstan changes, we segment radar images with *isolines*. An isoline refers to a line along which the radar echo magnitude is unchanged. The threshold of echo level is adaptive, such as radar echoes from low to high echo levels can be segmented. Features, such as the maximum of echo level $e_{\max}$, are then extracted from isolines and are used to define a statistical estimator for Galinstan level inside the microfluidic channel (see Fig. 8). The dynamic range $\Delta_{e_{\max}}$ associated with the estimator $e_{\max}$ is defined as follows:

$$\begin{aligned}\Delta_{e_{\max}} &= |e_{\max}(l_{\max}) - e_{\max}(l_{\min})| \\ &= \alpha_{e_{\max}} |l_{\max} - l_{\min}| \end{aligned} \quad (1)$$

where l denotes the level of Galinstan to be estimated $e_{\max}(l_{\min})$ and $e_{\max}(l_{\max})$ designate, respectively, the measured minimum and maximum of (co- or cross-polarized) echo level at the sensor location for the lowest ($l_{\min}$) and highest ($l_{\max}$) levels of Galinstan, and $\alpha_{e_{\max}}$ designates the mean sensitivity of the sensor derived from the statistical estimator $e_{\max}$. Measured dynamic range $\Delta_{e_{\max}}$ of the echo level and sensitivity $\alpha_{e_{\max}}$ are reported in Table I for $l_{\min} = 0.8$ mm and $l_{\max} = 3.0$ mm and for each polarization configuration p. The sensitivities are high for cross-polarized configurations (3.7 dB/mm for $p =$ VH and 4.5 dB/mm for $p =$ HV), and as expected, they are much lower in the co-polarized configurations (0.8 dB/mm for $p =$ VV and 2.4 dB/mm for $p =$ HH). However, the measured dynamic range is lower than the simulated RCS dynamic range. This difference can be explained by an impedance mismatch between the different parts of the printed structure due to misalignments of flanges. Such mismatch can be suppressed by the one-piece manufacturing of the entire sensor. Nevertheless, this sensor offers higher measurement dynamic and sensitivity than those reported in Table II. Moreover, the minimal detectable variation of the level of Galinstan $\delta_{\min}$ can also be derived from the standard deviation of the estimator $e_{\max}$. Values of $\delta_{\min}$ ranging from 3 to 84 μm depending on the sensitivity $\alpha_{e_{\max}}$ and the configuration p.

C. Measurement Uncertainty From 3-D Radar Images in the First Scenario

To characterize the precision of the radar measurement, we perform a step-by-step 3-D beamscanning with an angular step of 1° for angular sweeps of ±10° in azimuth and elevation. For each angular direction (θ, φ), $N = 108$ chirps are transmitted resulting in 108 beat frequency spectra. The resulting 3-D image is a matrix of size $N_\theta \times N_\varphi \times N_s$ where $N_\theta = 21$ and $N_\varphi = 21$ are the number of samples in

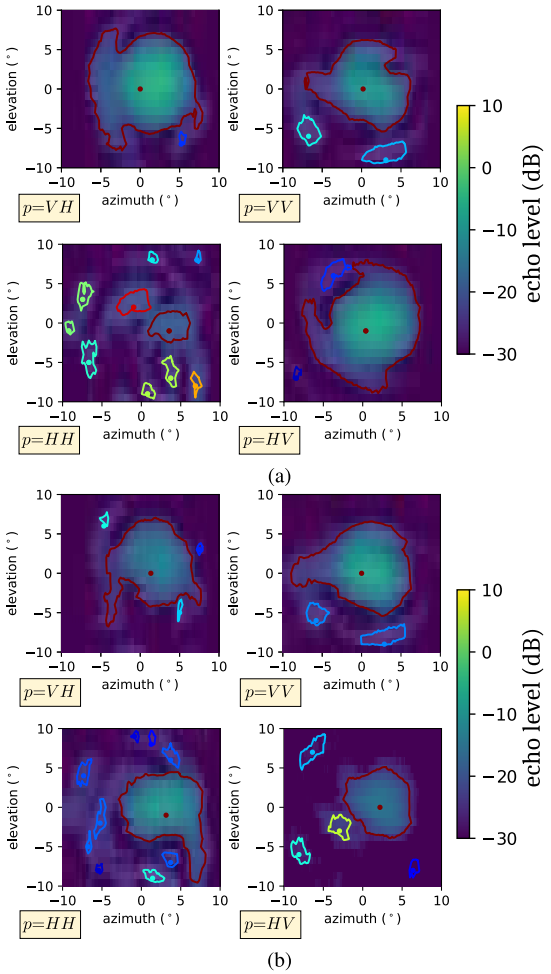

Fig. 7. Radar images in (θ, φ) at the reader-to-sensor position $R = 2.4$ m for various polarization configurations and for a level of Galinstan of (a) 0 mm and (b) 3.0 mm inside the channel.

azimuth and elevation, respectively. The noise level of a given voxel computed over N transmitted chirps is the standard deviation denoted by $\sigma_N(n_\theta, n_\varphi, n_R)$ where n_θ, n_φ, and n_R represent indices in the 3-D image in elevation, azimuth, and range, respectively. We also define the mean $\mu_N(n_\theta, n_\varphi, n_R)$ of echo level of the voxel over the N transmitted chirps. The measurement uncertainty (in linear scale) ε_N of the echo level in the voxel $(n_\theta, n_\varphi, n_R)$ is then given by

$$\varepsilon_N\left(n_\theta, n_\varphi, n_R\right) = \frac{\sigma_N\left(n_\theta, n_\varphi, n_R\right)}{\mu_N\left(n_\theta, n_\varphi, n_R\right)}. \tag{2}$$

As described in Section II, the radar echo level changes when the level of Galinstan in the microfluidic channel varies, and consequently, a high measurement precision requires low values of $\varepsilon_N(n_\theta, n_\varphi, n_R)$. The value of μ_N (in dB) as a function of ε_N is displayed in black color in Fig. 9(a) and (b) for $p =$ VV and VH, where each black dot represents a single voxel $(n_\theta, n_\varphi, n_R)$. As expected, the measurement uncertainty increases when the mean echo level decreases. Moreover, the *width* of the black curve in Fig. 9 is not constant and increases as μ_N decreases. We note that this width tends to be larger for co-polarized echo level compared with cross-polarized one. As an example, the mean relative uncertainty of ε_N denoted by $\overline{\varepsilon}$, equal to 1.3% when -15 dB $\leq \mu_N \leq -5$ dB and decreases

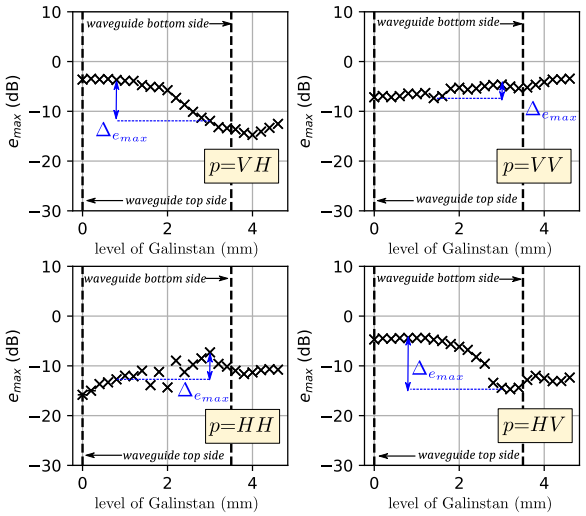

Fig. 8. Statistical estimator $e_{\max}$ as a function of the level of Galinstan inside the microfluidic channel with polarization configurations VH, VV, HH, and HV for a microfluidic passive sensor located at 2.4 m in front of the radar. The dynamic range $\Delta_{e_{\max}}$ is plotted from $l = 0.8$ to 3.0 mm.

TABLE I

SCENARIO 1: MEASURED CHARACTERISTICS OF THE PASSIVE MICROFLUIDIC SENSOR

p	$\Delta_{e_{max}}$ (dB)	$\alpha_{e_{max}}$ (dB/mm)
VH	8.2	3.7
VV	1.8	0.8
HH	5.4	2.4
HV	9.9	4.5

For l_{min} = 0.8mm and l_{max} = 3.0mm

TABLE II

PERFORMANCES COMPARISON BETWEEN CHIPLESS SENSORS INTERROGATED BY FM-CW RADARS

ref	sensitivity	dynamic range	parameters [a]
[6]	0.4dBm/°C	4dBm	copol; 2m ; 30GHz ; 23dBm
[7]	0.16dB/°C	4.4dB	copol; 2.4m ; 24GHz ; 53.5dBm
[9]	-0.2dB/%RH	9.5dB	xpol; 2.1m ; 24GHz ; 53.5dBm
[10]	3.8dB/bar	3.4dB	xpol; 4.8m ; 24GHz ; 38dBm
[11]	0.03dB/mbar	8.0dB	xpol; 3.0m ; 24GHz ; 48dBm
[29]	0.45dBsm/K	9dBsm	copol; 1.6m ; 30GHz ; 23dBm
this work	4.5dB/mm	9.9dB	xpol; 2.4m ; 24GHz ; 48dBm

[a] : polarization configuration; reading range; operating frequency; reader EIRP

to 2.7% when -20 dB $\leq \mu_N \leq -15$ dB for $p =$ VV. Values are similar for $p =$ VH and are reported in Table III.

We now extend the definition of the dynamic range reported in (1) to the statistical estimator e of echo level by

$$\Delta = |e(l_{\max}) - e(l_{\min})| = \alpha |l_{\max} - l_{\min}| \tag{3}$$

where $e(l_{\min})$ and $e(l_{\max})$ are the values of e for, respectively, the lowest $(l_{\min})$ and highest $(l_{\max})$ levels of Galinstan, and α denotes the measurement sensitivity of the sensor derived from the statistical estimator e. The measurement uncertainty of the echo level for the estimator e is then defined as

$$\varepsilon = \frac{\sigma}{\mu}. \tag{4}$$

According to (3) and (4) and assuming that e depends linearly on l between $l_{\min}$ and $l_{\max}$, the measurement precision δ of the estimation of the level of Galinstan inside the microfluidic

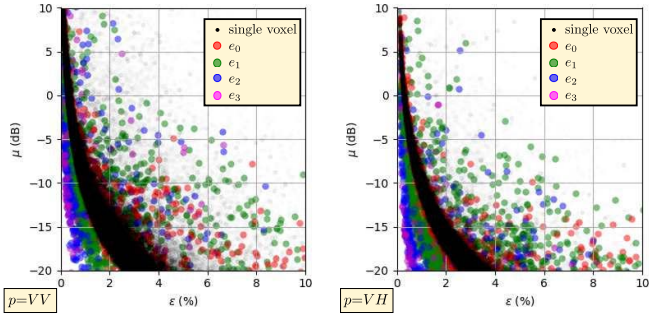

(a) (b)

Fig. 9. Mean echo level μ in dB scale as a function of the uncertainty ε in polarization configurations (a) VV and (b) VH for single voxels (black dots), as well as estimators e_0 (red circles), e_1 (green circles), e_2 (blue circles), and e_3 (magenta circles) derived from isolines.

channel may be derived as follows:

$$\delta = \frac{\sigma}{\alpha} = \varepsilon\mu \frac{|l_{\max} - l_{\min}|}{\Delta}. \quad (5)$$

Therefore, for the level of Galinstan l ranging from $l_{\min}$ to $l_{\max}$, the measurement precision δ is enhanced from the minimization of ε and maximization of Δ. In order to reduce the uncertainty ε given by (4), we propose to define the new statistical estimator e_w (with w an integer) from isolines computation and the spatial averaging within a window of size $(k+1) \times (k+1)$ voxels. The window is centered at the highest echo level $e_{\max}$ inside the isoline (i.e., $e_0 = e_{\max}$ in Section III-A). As an illustration, isolines are computed $N = 108$ times in a (θ, φ) plane at range $R = 2.5$ m and are plotted in cyan color in Fig. 10. Black to white colors represent the mean echo level calculated from 108 measurements. For each isoline, red crosses show the location of the highest echo level. Green, blue, and magenta squares indicate windows in which the averaging is performed for, respectively, e_1–e_3. We note that the averaging window of e_w may be larger than the surface enclosed by the isoline. To avoid large estimation inaccuracies, e_w is computed only if the window boundaries are inside the isoline.

To compare the uncertainty provided by all of these statistical estimators with one derived from (2), e_w is computed for $w = 0$, 1, 2, and 3 for all computed isolines. The mean echo level μ as a function of the uncertainty ε of the echo level measurement is plotted in Fig. 9 in red, green, blue, and magenta circles, respectively. It can be observed that the mean level of ε, as well as the width of the curve, decreases as the size of the window increases due to spatial averaging. However, as for single voxels, the uncertainty ε increases as the mean echo level μ decreases. To evaluate and compare these uncertainties, statistical features of ε are reported in Table III for -15 dB $\leq \mu \leq -5$ dB and -20 dB $\leq \mu \leq -15$ dB for e_w with $w = 0$, 1, 2, and 3. The mean of the uncertainty, denoted $\bar{\varepsilon}$, is computed between the 5th and 95th percentiles to remove extreme values. As an example for $p =$ VV and -15 dB $\leq \mu \leq -5$ dB, $\bar{\varepsilon}$ decreases and is of $\bar{\varepsilon} = 1.3\%$ for single voxels and 0.7% for e_3. We note that the estimator of $\bar{\varepsilon}$ for e_0 and e_1 does not decrease. It may be caused by some singular values of echo level from off-centered windows.

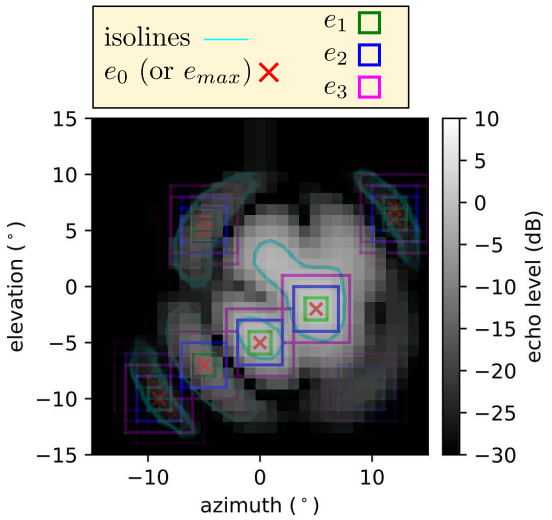

Fig. 10. Mean echo level over $N = 108$ measurements measured at a range $R = 2.5$ m for $p =$ VH. Plotted isolines (in cyan color) are computed N times and superimposed with windows of estimators e_0 (red crosses), e_1 (green squares), e_2 (blue squares), and e_3 (magenta squares).

TABLE III

ESTIMATORS CHARACTERISTICS

For -15dB$\leq \mu \leq$-5dB

	$\bar{\varepsilon}$ (%)		p5th (%)		p50th (%)		N_e	
p	VV	VH	VV	VH	VV	VH	VV	VH
voxels	1.3	1.3	0.6	0.6	1.2	1.2	50392	21896
e_0	1.2	1.2	0.6	0.6	1.1	1.2	779	512
e_1	1.5	1.6	0.3	0.4	0.8	0.8	481	289
e_2	0.9	0.9	0.2	0.2	0.4	0.5	165	99
e_3	0.7	0.8	0.1	0.2	0.3	0.6	62	23

For -20dB$\leq \mu \leq$-15dB

	$\bar{\varepsilon}$ (%)		p5th (%)		p50th (%)		N_e	
p	VV	VH	VV	VH	VV	VH	VV	VH
voxels	2.7	2.6	1.7	1.8	2.5	2.5	34618	26853
e_0	2.9	2.4	1.6	1.6	2.6	2.3	288	710
e_1	2.5	2.9	0.8	0.9	1.6	1.8	209	399
e_2	1.8	1.8	0.5	0.5	0.9	0.9	62	126
e_3	2.0	1.0	0.4	0.3	2.1	0.6	10	43

$\bar{\varepsilon}$: mean uncertainty between the 5th and the 95th percentiles
p5th: 5th percentile
p50th: 50th percentile
N_e: number of voxels or isolines between the 5th and the 95th percentiles

Consequently, we select the 50th percentile, denoted p50th, to represent the feature associated with spatial averaging. When the number of isolines N_e is significantly high (greater than 30), it can be observed that p50th decreases when w increases. Therefore, we can advantageously estimate the echo level with a lower uncertainty thanks to spatial averaging, and we may expect an enhancement of the precision of the estimated level of Galinstan. Finally, we note that uncertainties are similar for $p =$ VV and $p =$ VH, but the number of isolines (denoted by N_e in Table III) differs. Indeed, N_e is lower for $p =$ VH and -15 dB $\leq \mu \leq -5$ dB because the scene does not significantly depolarize the incident electric field transmitted by the radar. Therefore the uncertainty of the echo level measurement is not improved in the cross-polarized configurations, but the electromagnetic clutter is significantly reduced.

We propose now to analyze σ in order to derive for e_w, where $w = 0$, 1, 2, and 3 the estimated value of δ from (5). We assume that σ is constant, such as $\sigma = \sigma_{w,p50}$

gives the standard deviation of the estimator e_w at the 50th percentile. According to (4), $\mu_{w,p50}$ as a function of ε follows the hyperbolic law

$$\mu_{w,p50}(\varepsilon) = \frac{\sigma_{w,p50}}{\varepsilon}. \tag{6}$$

Such a model can be derived from Fig. 11 for $w = 0$, 1, 2, and 3 in red, blue, green, and magenta colors, respectively. Values of $\sigma_{w,p50}$ are computed from a parametric analysis based on a hyperbolic model and a minimization function from the Nelder–Mead algorithm [44]. As expected, $\sigma_{w,p50}$ decreases when the number of voxels n within the window increases. According to (5) and (6), the measurement precision of the Galinstan level estimation can be given by

$$\delta_{w,p50} = \frac{\sigma_{w,p50}}{\alpha_{w,p50}} = \sigma_{w,p50}\frac{|l_{\max} - l_{\min}|}{\Delta_{w,p50}}. \tag{7}$$

The measurement precision can be computed between two measurements m and $m+1$ within the dynamic range $\Delta_w[m] = |e_w[m+1] - e_w[m]|$. According to (7) for the measurement m, the precision can be estimated from the following relationship:

$$\delta_{w,p50}[m] = \sigma_{w,p50} \times \left|\frac{l[m+1] - l[m]}{e_w[m+1] - e_w[m]}\right|. \tag{8}$$

The measurement precision $\delta_{w,p50}$ is displayed in Fig. 12 as a function of the level of Galinstan for $w = 0$, 1, 2, and 3 and for $p =$ VV, VH, HV, and HH, respectively. As observed, the minimal measurement precision is observed for a level of Galinstan ranging from $l = 1.3$ to 3.0 mm where the dynamic range is maximal. It is reported in Table IV for $p =$ VV, VH, HV, and HH, and between $l = 1.3$ and 3.0 mm. The precision is lower than 100 μm for the estimator e_0 and decreases (as expected) when the size of the averaging window increases. As an example, $\delta_{2,p50}$ is lower than 20 μm for all polarization configurations. In some cases, there are missing estimations when the averaging window is outside of isoline boundaries. These situations are annotated with letters *na* in Table IV, and occur when $p =$ HH and $w > 1$. We conclude that the estimator e_w computed for various sizes of averaging window can be used to accurately estimate the level of Galinstan. However, the size of the window is limited by the boundaries of the isoline. Indeed, if it is too large, the averaging window may include undesirable echo levels from the electromagnetic clutter and degrade the measurement precision. Moreover, this precision model is mainly based on a step-by-step beamscanning with a static passive sensor. According to (8), the temperature precision of the sensor from the estimator e_w between two measurements m and $m+1$ is

$$\begin{aligned}\delta_{T_{w,p50}}[m] &= \delta_{w,p50}[m] \times \frac{\delta_T}{\delta_l} \\ &= \left|\frac{l[m+1] - l[m]}{e_w[m+1] - e_w[m]}\right| \times \frac{\sigma_{w,p50} \times S_c}{\alpha_T \times V_{\text{tank}}}.\end{aligned} \tag{9}$$

If we consider the temperature sensitivity $(\delta_l)/(\delta_T) = 5.9$ μm/°C calculated previously in Section II with $V_{\text{tank}} = 10$ mm^3, the mean temperature precision of the sensor for $p =$ VH would be $\delta_{T_{0,p50}} = 2.9$ °C and $\delta_{T_{3,p50}} = 0.7$ °C. These results will be compared in future works with true temperature measurements. One must ensure that the Galinstan flows correctly through the channel with the expected dilation coefficient. Moreover, repeatability tests must be performed to ensure that the meniscus level goes back to its initial position ($l = 0$ mm) without leaving Galinstan residues in the channel.

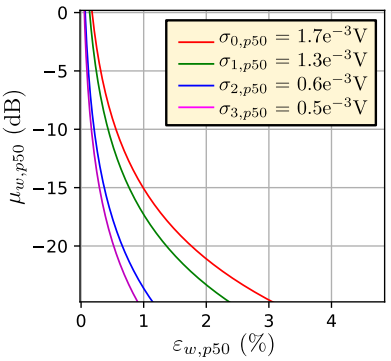

Fig. 11. Noise model estimated from the 50th percentile of ε for $w = 0$, 1, 2, and 3, respectively, in red, blue, green, and magenta colors.

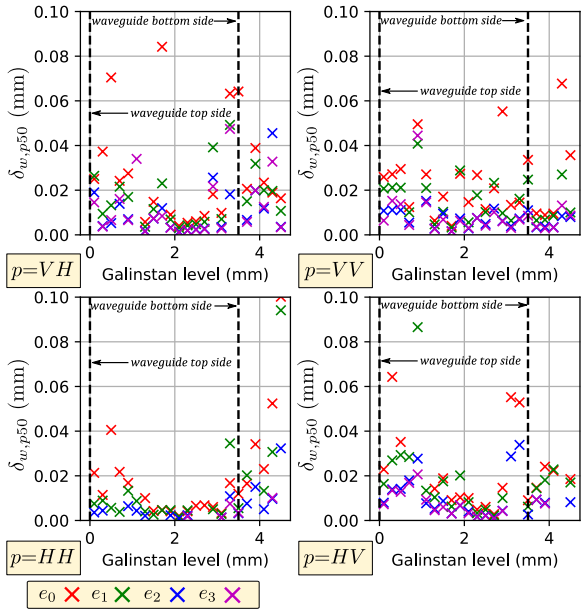

Fig. 12. Estimated precision of the measurement as a function of the level of Galinstan for e_0–e_3 indicated, respectively, by red, green, blue, and magenta crosses.

TABLE IV
ESTIMATED MEASUREMENT PRECISION IN μM

	mean / min / max (μm)			
p	VV	VH	HV	HH
$\delta_{0,p50}$	16 / 4 / 27	17 / 4 / 84	10 / 3 / 19	6 / 2 / 10
$\delta_{1,p50}$	12 / 3 / 28	7 / 3 / 23	9 / 3 / 20	4 / 2 / 5[a]
$\delta_{2,p50}$	6 / 2 / 12	4 / 1 / 11	4 / 1 / 9	6 / 1 / 15[b]
$\delta_{3,p50}$	6 / 2 / 11	4 / 1 / 9	4 / 1 / 7	na

$\delta_{w,p50}$ is computed between a level of Galinstan between 1.3mm and 3.0mm inside the waveguide structure.
[a] and [b]: respectively 2 and 4 estimations are removed because the averaging window is outside of isoline boundaries
na : the averaging window is outside of isoline boundaries for all measurements

D. Second Scenario: Long-Range Remote Reading of the Microfluidic Sensor

We now place the microfluidic sensor in a basement of a building at distances of 5.2, 9.9, and 14.8 m from the radar. For each sensor position, the level l of Galinstan

ranges from 0 to 3.2 mm. The experimental setup and the schematic of the scenario are shown in Fig. 13. Isolines at the location of the sensor are generated and the estimator $e_{\max}$ is plotted as a function of the Galinstan level. Results are reported in Fig. 14 in cross-polarization configurations for the three above-mentioned radar-to-sensor distances. Values of $e_{\max}$ obtained from the first scenario (see Section III-A) are also displayed for comparison purposes. We observe that the dynamic range, as well as the mean echo level, vary with the radar-to-sensor distance. The three relevant sensor descriptors, namely the full-scale dynamic range $\Delta_{e_{\max}}$, sensitivity $\alpha_{e_{\max}}$, and mean echo level $\overline{e_{\max}}$ are reported in Table V for the level of Galinstan ranging from $l_{\min} = 0.8$ mm to $l_{\max} = 3.0$ mm. We observe that the full-scale dynamic range, and consequently the sensitivity, decreases as the radar-to-sensor separation distance increases. This reduction is not due to the attenuation of the electromagnetic power density with the distance (because the radar system integrates a R^2 filter correction) but originates from the degradation of the spatial resolution of the beamscanning at larger distances. A collateral effect of such dynamic range and sensitivity degradation is the decrease of the mean echo level as the radar-to-sensor separation distance increases. Moreover, for long detection ranges, the electromagnetic backscattering from objects in the vicinity of the sensor may interfere with the electromagnetic field backscattered by the sensor and may participate in the measured echo level. The result of such interference is visible for $p = \text{HV}$ at the range of 14.8 m. At such radar-to-sensor separation distance and polarization configuration, the echo level of the electromagnetic clutter (due to the table supporting the sensor) prevents the wireless detection of the sensor. Inversely, at this distance and for $p = \text{VH}$, the electromagnetic clutter is mitigated. Therefore the sensor is detectable and the level of Galinstan can be remotely estimated, but with a lower measurement sensitivity (1.2 dB/mm) than that obtained at the shorter distance of $R = 2.4$ m (3.9 dB/mm). In addition, we observe that statistical estimator $e_{\max}$ as a function of Galinstan level may also vary with different sensitivities (for example when the level ranges from $l = 2$ to 3.2 mm with $p = \text{HV}$). We must investigate the reasons for this low and unexpected variability. Future works will consist of compensating for the observed reader-to-sensor dependency. Calibrations of the radar setup from canonical targets for various distances may compensate for this effect. The propagation channel may also affect the sensitivity, so we must ensure that the calibration is applicable to different environments. Passive sensor localization is therefore mandatory to retrieve the radar-to-sensor distance and then to apply a calibration corresponding to the correct reader-to-sensor distance.

IV. Electromagnetic Clutter Mitigation and Passive Sensor Localization

In this section, we propose a novel technique to 3-D localize passive sensor echoes in cluttered environments and for various radar-to-sensor separation distances. More specifically, we exploit the electromagnetic signature of the structural electromagnetic backscattering mode of sensors for various polarization configurations. The structural backscattering mode is very useful to localize the sensor and unlike the sensing backscattering mode, it does not depend on the level of Galinstan. Therefore, the resulting isolines in radar images may have specific shapes. The structural backscattering mode originates here from both the sensor's metallic structure and its surroundings.

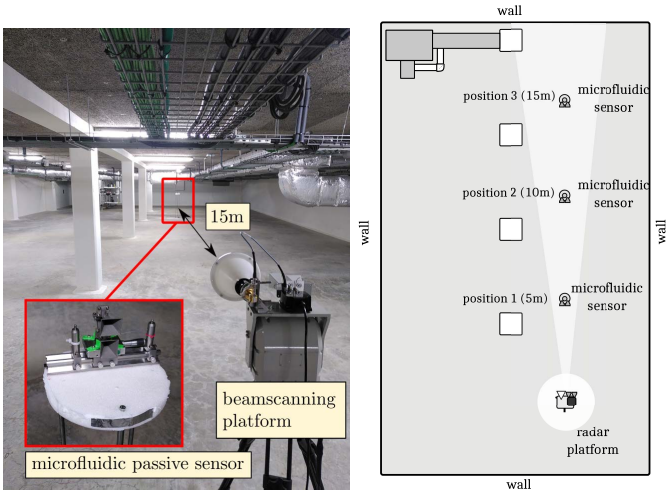

Fig. 13. (a) Photograph of the passive microfluidic sensor at 15 m from the beamscanning platform and (b) illustration of scenario 2.

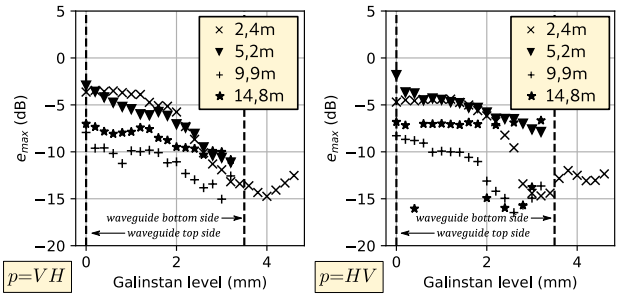

Fig. 14. Estimator $e_{\max}$ as a function of the level of Galinstan for $p = \text{VH}$ and HV at a radar-to-sensor distance of 2.4 m (crosses), 5.2 m (down triangles), 9.9 m (plus signs), and 14.8 m (stars).

TABLE V
Estimator Characteristics for Different Ranges of Interrogation

	$\Delta_{e_{max}}$(dB)		$\alpha_{e_{max}}$(dB/mm)		$\overline{e_{max}}$(dB)	
p	VH	HV	VH	HV	VH	HV
2.4m	8.2	9.9	3.7	4.5	-8.5	-8.7
5.2m	5.4	3.3	2.4	1.5	-6.7	-5.3
9.9m	3.8	4.9	1.7	2.2	-11.2	-11.7
14.8m	2.0	na	0.9	na	-8.7	na

For l_{min} = 0.8mm and l_{max} = 3.0mm

A. Clutter Mitigation From Isolines Computation

We build reference images of the structural backscattering mode of the passive sensor based on the 24 beamscannings performed in scenario 1 and for various levels of Galinstan. The structural mode is located at the distance of $R = 2.3$ m from the radar, that is, 10 cm ahead of the sensing backscattering mode. Reference images for each polarization configuration are computed by performing a so-called *principal component analysis* (PCA) [45] on the 24 radar images for $R = 2.3$ m. The first component of the PCA is kept and

has variance ratios of 50.7%, 42.2%, 38.1%, and 51.3% for, respectively, p = VV, VH, HV, and HH. Variance ratios of other components do not exceed 8%. The resulting images are displayed in Fig. 15 with the computed isolines. In a co-polarized configuration, the radar image is composed of one segmented radar echo, while in a cross-polarized configuration, four radar echoes of lower magnitudes are observed and segmented. This result originates from the geometry of the passive sensor structure and of its support platform (a table in our experiment), and it may be used to estimate the 3-D position of the passive sensor in different scenarios. For this purpose, we determine a selection of geometrical properties of isolines that may help to mitigate the electromagnetic clutter. The proposed selection, based on the observation of radar echoes in Fig. 15, is performed in four steps.

1) Step n°1: Selection of radar images in the four polarization configurations at a given distance R.
2) Step n°2: Computation of isolines. One must select a rather low initial echo level threshold to segmentate all radar echoes (−30 dB here). Other criteria for the selection may be used to remove noise, such as the minimal area per isoline (here 5 px^2), the maximal number of local peaks of echo level inside each isoline (here only one local peak), or the maximal area (here 250 px^2 is chosen to avoid too large isolines that may alter the structural backscattering mode identification). A more detailed description of the algorithm is reported in [46].
3) Step n°3: Selection of each isoline in co-polarized configuration p = VV (respectively, p = HH) and computation of a circle in which the center coordinates are those of the isoline barycenter. The perimeter of the circle is 1.5 greater than the perimeter of the isoline. We choose a factor of 1.5 such as the circle intersects with other isolines that are placed nearby.
4) Step n°4: In the radar image in cross-polarized configuration p = VH (respectively p = HV), selection of all isolines that intersect with the circle. If the number of intersections is higher than (or equal to) 3, we select the isolines. The final selection is composed of one isoline in the co-polarized configuration associated with at least three isolines in the cross-polarized configuration (note that four isolines intersect in Fig. 15, but the criterion of three intersections is chosen to provide a margin).

As an illustrative example, we apply the four steps to the radar images of scenario 2 at the distance of 5.1 m and for p = VV and VH. At this distance is located the structural backscattering mode of the passive sensor. Results are displayed in Fig. 16 where magenta and cyan colors indicate isolines for p = VV and VH, respectively. The circles are plotted in dashed lines. When the selection process is applied (see right figure), only one isoline in the co-polarized configuration with four isolines in the cross-polarized configuration are selected.

The impact of the proposed isolines selection can be evaluated by computing the sensor-to-clutter radar echoes ratio

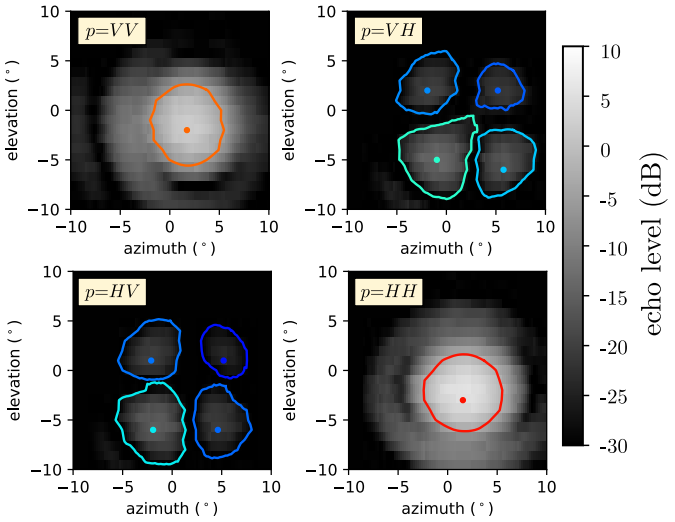

Fig. 15. Reference radar images of the structural backscattering mode for the four polarization configurations (scenario 1 for a radar-to-sensor separation distance of 2.3 m).

defined by

$$\Lambda_p = \frac{N_{s,p}}{N_{s,p} + N_{c,p}} \tag{10}$$

where $N_{s,p}$ is the number of isolines generated by the sensor structural backscattering mode and $N_{c,p}$ is the number of isolines generated by undesirable electromagnetic clutter. Note that values of Λ_p are large when they are compared within a similar scanned volume. In this work, the scanned volume V_{scan} is one of a sphere part given by

$$V_{\text{scan}} = \frac{1}{3}\left(R_{\max}^3 - R_{\min}^3\right) \times (\varphi_{\max} - \varphi_{\min}) \times (\sin(\theta_{\max}) - \sin(\theta_{\min})). \tag{11}$$

Minimal and maximal azimuth angles are $\varphi_{\min} = -10°$ and $\varphi_{\max} = 10°$, respectively, as well as for minimal and maximal elevations angles $\theta_{\min}$ and $\theta_{\max}$. Minimal detection range is $R_{\min} = 0$ and the maximal range $R_{\max}$ depends on the number of range bins $N_R = 256$ (see Section III-A) and the depth resolution d. However, the delay line that connects the radar front-end to the T_x lens antenna has an electrical length $d_{\text{off}} = 1$ m that decreases the maximal interrogation distance. Indeed, the distance $R_{\max}$ is given by $d \times N_R - d_{\text{off}} =$ 18.2 m. The scanned volume is then $V_{\text{scan}} = 243.6$ m^3. Values of Λ_p, $N_{s,p}$, and $N_{c,p}$ are reported in Table VI for the 24 beamscannings performed in scenario 1 (see Section III-A) and 17 beamscannings in scenario 2 ($R = 5.1$ m) before and after isoline selection in the scanned volume. Values of $N_{s,p}$ are computed by measuring the ground-truth position of the structural backscattering mode and counting isolines inside a restricted volume. We first compare the values of Λ_p obtained from scenario 1 with those derived from scenario 2. Λ_p is found to be higher in scenario 2 because the basement of the building is larger than the laboratory room and contains less reflective targets. We can also compare values of Λ_p before and after isolines selection. As observed, Λ_p increases after the selection (from 2 to 8 times higher) because the electromagnetic clutter is drastically reduced from applying such selection. We note that after the isoline selection, $N_{s,\text{VV}} =$

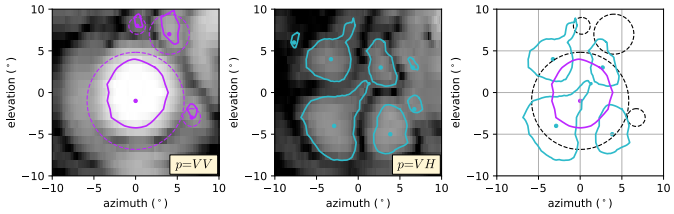

Fig. 16. Isolines computed at the distance of the structural backscattering mode (from scenario 2 at 5.1 m) for p = VH (cyan color) and p = VV (magenta color). Selected isolines are superimposed on the right image.

TABLE VI
CLUTTER MITIGATION EFFECT FROM ISOLINES SELECTION

p	*before selection*			*after selection*		
	$N_{s,p}$	$N_{c,p}$	Λ_p	$N_{s,p}$	$N_{c,p}$	Λ_p
VV	24	6.0E4	4.0E-4	24	7.4E3	3.2E-3
VH	96	6.8E4	1.4E-3	96	3.6E4	2.7E-3
HV	96	6.6E4	1.4E-3	96	3.1E4	3.0E-3
HH	24	5.6E4	4.2E-4	24	6.7E3	3.5E-3

Results obtained from 24 measurements in scenario 1 - microfluidic sensor at range R=2.2m

p	*before selection*			*after selection*		
	$N_{s,p}$	$N_{c,p}$	Λ_p	$N_{s,p}$	$N_{c,p}$	Λ_p
VV	29	2.8E4	1.0E-3	17	8.2E2	2.0E-2
VH	68	2.6E4	2.5E-3	68	3.5E3	1.8E-2
HV	76	2.3E4	3.2E-3	68	2.9E3	2.2E-3
HH	18	3.0E4	5.9E-4	17	7.4E2	2.2E-2

Results obtained from 17 measurements in scenario 2 - microfluidic sensor at range R=5.1m

$N_{s,\mathrm{HH}}$ corresponds to the number of beamscannings per scenario. Moreover, $N_{s,\mathrm{VH}} = N_{s,rmHV} = 4 \times N_{s,\mathrm{VV}}$. Isolines associated with the passive sensor structural backscattering mode are not mitigated and one isoline in the co-polarized configuration is combined with four isolines in the cross-polarized configuration. Consequently, the proposed isolines selection allows for achieving efficient clutter mitigation. However, such mitigation is not sufficient to find the position of the sensor. For each beamscanning, more than 300 isolines in scenario 1 (50 in scenario 2) from the clutter are not mitigated in the co-polarized configuration. The localization of the sensor can be now achieved from a new technique reported in Section IV-B.

B. Passive Sensor Detection and Localization Among the Electromagnetic Clutter

In the previous section, the clutter is mitigated by selecting isolines according to their geometrical properties in co-polarization and cross-polarization. Such selection is found to be not sufficient to estimate the position of a passive sensor. Therefore we propose here to determine the 3-D position of the passive sensor from a new technique based on the comparison of selected isolines with reference isolines displayed in Fig. 15. From such comparison, the shape of the selected isolines is extracted and scores of similarity with the shape of reference isolines are computed. The algorithm to compute the similarity score is composed of the following steps.

1) Step n°1: Selection of isolines for all polarization configurations at a given distance R from the radar. For p = VV (respectively, HH), we select one single isoline; for p = VH (respectively, HV), we select a set of at least three isolines as done in Section IV-A.
2) Step n°2: For p = VV (respectively, HH), translation of the selected isoline such as its barycenter has the same direction (θ, φ) than one of the reference isoline barycenter.
3) Step n°3: Identical translation for p = VH (respectively, HV).
4) Step n°4: Computation of surfaces enclosed by the selected isolines (we denote these surfaces $\mathcal{S}$ for selected isolines and $\mathcal{S}_{\mathrm{ref}}$ for reference isolines).
5) Step n°5: Computation of the intersection of isolines and union between isolines. For this purpose, we define $\cap(\mathcal{S}_p, \mathcal{S}_{p,\mathrm{ref}})$ and $\cup(\mathcal{S}_p, \mathcal{S}_{p,\mathrm{ref}})$ the surfaces of, respectively, intersection and union between isolines of surfaces $\mathcal{S}_p$ and $\mathcal{S}_{p,\mathrm{ref}}$ in polarization configuration p.
6) Step n°6: Computation of the similarity score between isolines sharing the same polarization configuration p, defined by $s_p = (\cap(\mathcal{S}_p, \mathcal{S}_{p,\mathrm{ref}}))/(\cup(\mathcal{S}_p, \mathcal{S}_{p,\mathrm{ref}}))$. If selected and reference isolines are similar, $s_p = 1$. If they do not intersect, $s_p = 0$.
7) Step n°7: Computation of the mean similarity score of the selected isolines defined by: $\xi = (1/4)(s_{\mathrm{VV}} + s_{\mathrm{VH}} + s_{\mathrm{HV}} + s_{\mathrm{HH}})$ and calculation of the maximal value of ξ within the scanned volume. The mean range, azimuth, and elevation of the corresponding set of isolines are finally computed.

The proposed steps are illustrated in Fig. 17. Reference isolines computed in Section IV-A for scenario 1 are plotted in Fig. 17(a) in red color for the four polarization configurations. Tested isolines are isolines from a structural backscattering mode of the sensor in scenario 2 at the distance R of 5.1 m. Black solid and dashed lines represent tested isolines before and after the translation. Union and intersection between reference and tested isolines are then computed and plotted on Fig. 17(b), respectively, with blue solid and green dashed lines. In the co-polarized configuration, green and blue isolines are very similar and similarity scores are close to the maximal value ($s_{\mathrm{VV}} = 88\%$ and $s_{\mathrm{HH}} = 94\%$). In the cross-polarized configuration, the similarity score is lower ($s_{\mathrm{VH}} = 68\%$ and $s_{\mathrm{HV}} = 53\%$) because sets of four isolines do not match perfectly. The mean similarity score of these isolines is finally $\xi = 75\%$. Performances of the algorithm are reported in Table VII for all radar measurements performed in each scenario. We consider a detection as true when the detected range is at a distance of ± 10 cm from the ground-truth distance of the structural backscattering mode. Only statistics of true detections are computed and σ_R is lower or equal to the radar depth resolution d since true detections are always observed within a range variation of $\pm d$. We observe that there are only three false detections over a total of 75 radar measurements. Best results are then obtained from scenario 1, with a mean similarity score over 24 measurements $\mu_\xi = 83\%$. Such a high value of ξ is expected since reference isolines are built with radar images of scenario 1 (see Section IV-A). We note that ξ decreases in scenario 2, but passive sensor detection is still possible. The three false detections for R = 14.7 m are explained by poor similarity scores in cross-

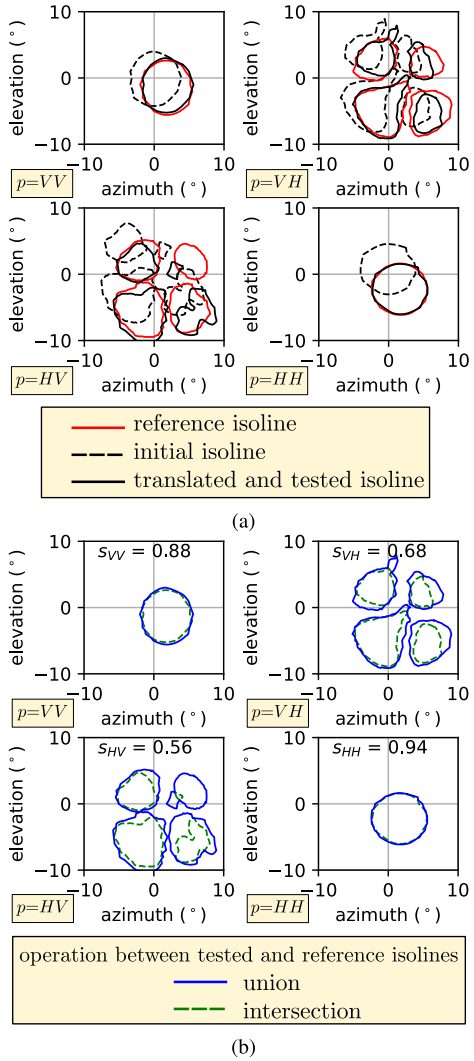

Fig. 17. Illustration of the passive sensor localization algorithm (scenario 2 at 5.1 m). (a) Red and black colors plotted are, respectively, reference and tested isolines. (b) Union and intersection of reference and tested isolines are plotted, respectively, in blue and green colors. The score s_p is computed for each polarization configuration.

polarized configuration, as illustrated in Fig. 18. In Fig. 18(a), red and black colors are superimposed reference and tested isolines, respectively. We observe that tested isolines do not match in cross-polarized configuration. As a result, union and intersection of isolines, displayed in Fig. 18(b), generate low similarity scores in cross-polarized configuration with $s_{\mathrm{VH}} = 18\%$ and $s_{\mathrm{HV}} = 29\%$, and a mean similarity score $\xi = 50\%$. Despite these few false detections, these results are very encouraging.

C. Passive Sensor Localization for Different Angles of Interrogation

The localization algorithm proposed in Section IV-B is now applied to scenario 3 where the passive microfluidic sensor is translated along the x-axis as depicted in Fig. 19. Five positions are tested with a translation varying from 10 to 50 cm and a step of 10 cm along the x-axis. For each position, the radar performs the beamscanning with azimuth and elevation angles varying from $-10°$ to $+10°$ on each side

TABLE VII
LOCALIZATION ESTIMATION

scenario	(1)	(2)		
true range (m)	2.2	5.1	9.8	14.7
true detections	24	17	17	14
false detections	0	0	0	3
μ_R (m)	2.2	5.1	9.7	14.7
σ_R (cm)	$\leq$7.5	$\leq$7.5	$\leq$7.5	$\leq$7.5
μ_θ (°)	-1.9	0.6	1.7	1.9
σ_θ (°)	0.4	0.5	0.3	0.2
μ_φ (°)	1.6	0.0	-0.5	-0.7
σ_φ (°)	0.1	0.1	0.1	0.1
μ_ξ	0.84	0.74	0.60	0.53
σ_ξ	0.05	0.02	0.04	0.01

μ_x and σ_x denote respectively the mean and standard deviation of the x parameter.

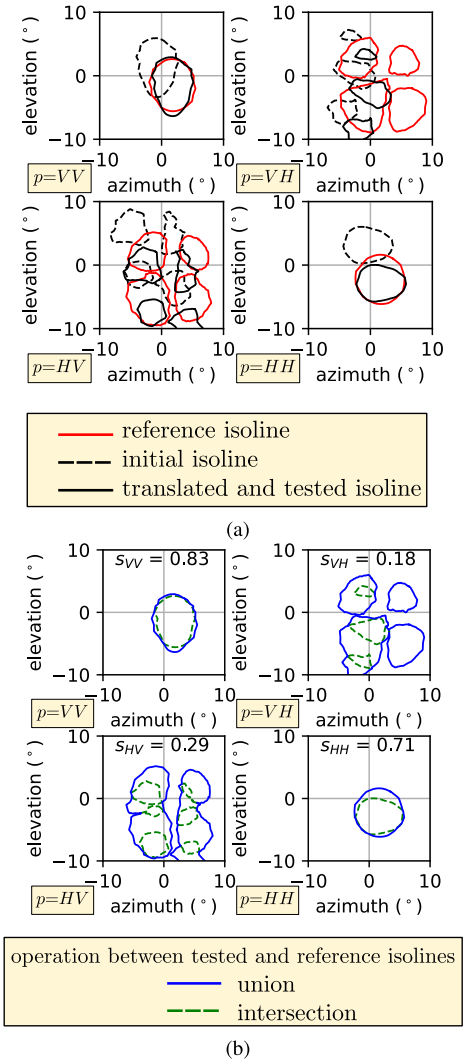

Fig. 18. Illustration of the passive sensor localization algorithm (scenario 2 at 14.7 m). (a) Red and black colors plotted are, respectively, reference and tested isolines. (b) Union and intersection of reference and tested isolines are plotted, respectively, in blue and green colors. The score s_p is computed for each polarization configuration.

of the passive sensor location, with an azimuth angle offset $\varphi(x)$ that depends on the x translation. Localization results are reported in Table VIII for the five positions. We observe that ξ tends to decrease with $\varphi(x)$ and we may expect false detections for values of $\varphi(x)$ lower than $-15°$. The maximum similarity score is detected at the passive sensor position

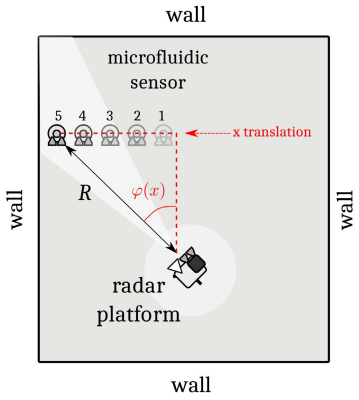

Fig. 19. Schematic of scenario 3 (laboratory room) when the passive microfluidic sensor is translated along the x-axis. The azimuth angle offset $\varphi(x)$ is enlightened in red color for the five annotated positions of the microfluidic sensor.

TABLE VIII
LOCALIZATION RESULTS FOR VARIOUS AZIMUTH ANGLE OFFSETS

x-axis translation (cm)	10	20	30	40	50
true range (m)	2.2	2.2	2.2	2.2	2.3
$\varphi(x)$ (°)	-2.6	-5.2	-7.8	-10.3	-12.8
detection peak	1st	2nd	1st	1st	1st
R(m)	2.3	2.3	2.4	2.3	2.4
θ (°)	-1.0	-1.5	-0.5	-2.0	-1.5
φ (°)	-0.7	-4.5	-6.4	-8.3	-10.0
ξ	0.77	0.64	0.70	0.57	0.68

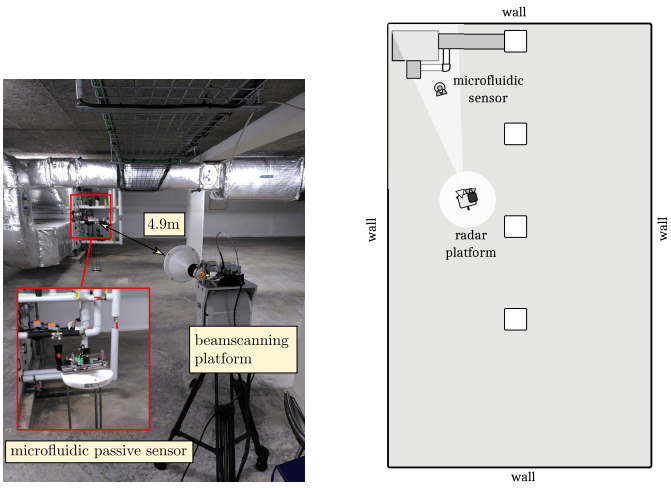

(a) (b)

Fig. 20. (a) Photograph of the passive microfluidic sensor at 5.0 m from the beamscanning platform in the vicinity of reflective targets and (b) illustration of scenario 4.

except for an x-axis translation of 20 cm, where $\xi = 64\%$ is the second maximum similarity score. For this particular case, the maximum similarity score is detected at 4.85 m with $\xi = 67\%$ and corresponds to a false target. The number of false targets may be reduced by defining more specific and unique isoline shapes.

D. Minimum Permissible Similarity Score

The localization performance of the structural backscattering mode depends both on the nature of the scene illuminated by the radar and the sensor location. In each scenario, the minimum similarity score must be reached in order to perform successful localization and avoid false detections. To evaluate

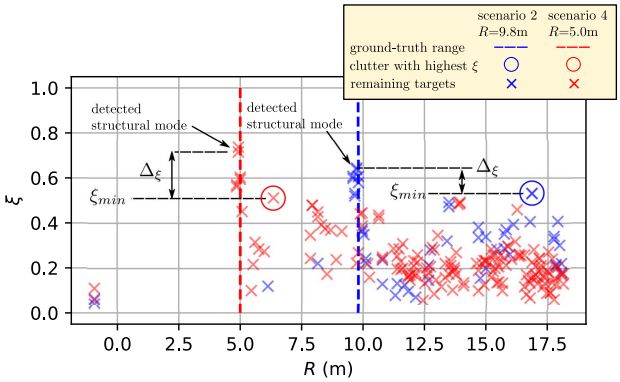

Fig. 21. Similarity score ξ of remaining targets as a function of the range R for scenario 2 (blue crosses) and scenario 4 (red crosses).

the minimum similarity score, we propose a fourth scenario of measurement performed in the same basement used in scenario 2. The difference is that the passive microfluidic sensor is located at a distance of 5.0 m from the radar and placed near reflective targets (see Fig. 20). The beamscanning performed in such scenario generates, after the isolines selection, a sensor-to-clutter radar echoes ratio $\Lambda_{VV} = 7.7e{-}3$, which is about $3\times$ lower than one obtained in scenario 2 (see Table VI). This is due to the presence of reflective metallic targets, such as pipes and large structures, near the sensor. We then compare the computed similarity scores ξ of scenarios 2 and 3 for $R = 9.8$ m. Values of ξ as a function of the range R are plotted in Fig. 21 for two beamscannings. Similarity scores of remaining targets for scenarios 2 and 3 are plotted in this figure by using, respectively, blue and red crosses. Vertical colored dashed lines represent the ground-truth distance of the sensor structural backscattering mode from the radar in scenario 2 (blue color) and scenario 3 (red color). The structural backscattering mode is detected in both scenarios with $\xi_{\max} = 64\%$ and 73% in scenario 3. However, values of ξ for other isolines are different. In scenarios 2 and 3, clutters with the highest similarity scores are highlighted with, respectively, blue and red circles and they are defined here as the *minimum permissible similarity score* $\xi_{\min}$. We have $\xi_{\min} = 53\%$ for scenario 2 with a margin error without false detections $\Delta_\xi = \xi_{\max} - \xi_{\min}$ of 11%. For scenario 4, $\xi_{\min} = 51\%$ with $\Delta_\xi = 22\%$. Despite a higher number of reflective targets, the localization of the passive sensor is easier in scenario 4, mainly because the radar-to-sensor distance is shorter.

V. CONCLUSION

The proposed wireless and passive sensor shows very encouraging results for the first prototype because of its large measurement dynamic range. A dynamic range of 9.9 dB and sensitivity of 4.5 dB/mm can be achieved at a remote reading distance of 2.4 m. With a well-defined statistical estimator, the measurement uncertainty is lower than 10 μm. The sensitivity decreases to 0.9 dB/mm at a remote reading distance of 14.8 m. The localization technique based is successfully achieved for various scenarios with only three false detections on 75 measurements.

Based on these results, works are now focused on the additive fabrication of the sensor with sintering laser melting in one

single piece in order to remove the flanges and consequently, to suppress impedance mismatch between the different parts of the printed structure due to misalignments. Moreover, investigations are ongoing to extend the proposed polarimetric radar imaging technique to locate and identify multiple sensors in cluttered environments for reading distances up to a few tens of meters.

REFERENCES

[1] F. Requena, N. Barbot, D. Kaddour, and E. Perret, "Combined temperature and humidity chipless RFID sensor," *IEEE Sensors J.*, vol. 22, no. 16, pp. 16098–16110, Aug. 2022.

[2] P. Fathi, S. Bhattacharya, and N. C. Karmakar, "Dual-polarized keratin-based UWB chipless RFID relative humidity sensor," *IEEE Sensors J.*, vol. 22, no. 3, pp. 1924–1932, Feb. 2022.

[3] F. Paredes, C. Herrojo, R. Escudé, E. Ramon, and F. Martín, "High data density near-field chipless-RFID tags with synchronous reading," *IEEE J. Radio Freq. Identificat.*, vol. 4, no. 4, pp. 517–524, Dec. 2020.

[4] N. Barbot and E. Perret, "Impact of the polarization over the read range in chipless RFID," in *Proc. IEEE Int. Conf. RFID Technol. Appl. (RFID-TA)*, Oct. 2021, pp. 139–141.

[5] N. Barbot, O. Rance, and E. Perret, "Classical RFID versus chipless RFID read range: Is linearity a friend or a foe?" *IEEE Trans. Microw. Theory Techn.*, vol. 69, no. 9, pp. 4199–4208, Sep. 2021.

[6] S. Bouaziz, F. Chebila, A. Traille, P. Pons, H. Aubert, and M. M. Tentzeris, "Novel microfluidic structures for wireless passive temperature telemetry medical systems using radar interrogation techniques in Ka-band," *IEEE Antennas Wireless Propag. Lett.*, vol. 11, pp. 1706–1709, 2012.

[7] D. Henry, H. Aubert, and P. Pons, "3D scanning and sensing technique for the detection and remote reading of a passive temperature sensor," in *IEEE MTT-S Int. Microw. Symp. Dig.*, May 2016, pp. 1–4.

[8] J. G. Hester and M. M. Tentzeris, "Inkjet-printed Van-Atta reflectarray sensors: A new paradigm for long-range chipless low cost ubiquitous smart skin sensors of the Internet of Things," in *IEEE MTT-S Int. Microw. Symp. Dig.*, May 2016, pp. 1–4.

[9] D. Henry, J. G. D. Hester, H. Aubert, P. Pons, and M. M. Tentzeris, "Long-range wireless interrogation of passive humidity sensors using Van-Atta cross-polarization effect and different beam scanning techniques," *IEEE Trans. Microw. Theory Techn.*, vol. 65, no. 12, pp. 5345–5354, Dec. 2017.

[10] D. Henry, T. Marchal, J. Philippe, P. Pons, and H. Aubert, "Classification of radar echoes for identification and remote reading of chipless millimeter-wave sensors," *IEEE Trans. Microw. Theory Techn.*, vol. 69, no. 1, pp. 926–937, Jan. 2021.

[11] T. Marchal, D. Henry, P. Pons, and H. Aubert, "Wireless measurement of the pressure from the Ka-band radar echo of a 3D-printed microfluidic depolarizing sensor," in *IEEE MTT-S Int. Microw. Symp. Dig.*, Jun. 2021, pp. 173–175.

[12] E. A. Rojas-Nastrucci, T. Weller, V. L. Aida, F. Cai, and J. Papapolymerou, "A study on 3D-printed coplanar waveguide with meshed and finite ground planes," in *Proc. IEEE 15th Annu. Wireless Microw. Technol. Conf. (WAMICON)*, Jun. 2014, pp. 1–3.

[13] A. Delage et al., "Aerosol jet printing of millimeter wave transmission lines on 3D ceramic substrates made by additive manufacturing," in *IEEE MTT-S Int. Microw. Symp. Dig.*, Jun. 2018, pp. 1557–1560.

[14] M. M. Abdin, W. J. D. Johnson, J. Wang, and T. M. Weller, "W-band finite ground coplanar waveguide (FG-CPW) using laser enhanced direct-print additive manufacturing (LE-DPAM)," in *IEEE MTT-S Int. Microw. Symp. Dig.*, Jun. 2019, pp. 1213–1216.

[15] S. Roy, M. B. Qureshi, S. Asif, and B. D. Braaten, "A model for 3D-printed microstrip transmission lines using conductive electrifi filament," in *Proc. IEEE Int. Symp. Antennas Propag. USNC/URSI Nat. Radio Sci. Meeting*, Jul. 2017, pp. 1099–1100.

[16] J. Sorocki, I. Piekarz, S. Gruszczynski, K. Wincza, and J. Papapolymerou, "Application of additive manufacturing technologies for realization of multilayer microstrip directional filter," in *Proc. IEEE 68th Electron. Compon. Technol. Conf. (ECTC)*, May 2018, pp. 2382–2388.

[17] V. Laur, J. P. Gouavogui, and B. Balde, "C-band hybrid 3-D-printed microwave isolator," *IEEE Trans. Microw. Theory Techn.*, vol. 69, no. 3, pp. 1579–1585, Mar. 2021.

[18] S. Kim, H. Aubert, and M. M. Tentzeris, "An inkjet-printed flexible broadband coupler in substrate integrated waveguide (SIW) technology for sensing, RFID and communication applications," in *IEEE MTT-S Int. Microw. Symp. Dig.*, Jun. 2014, pp. 1–4.

[19] S. Moscato et al., "Additive manufacturing of 3D substrate integrated waveguide components," *Electron. Lett.*, vol. 51, no. 18, pp. 1426–1428, Sep. 2015. [Online]. Available: https://ietresearch.onlinelibrary.wiley.com/doi/abs/10.1049/el.2015.2298

[20] G. M. Rocco et al., "3-D printed microfluidic sensor in SIW technology for liquids' characterization," *IEEE Trans. Microw. Theory Techn.*, vol. 68, no. 3, pp. 1175–1184, Mar. 2020.

[21] P. Booth and E. V. Lluch, "Enhancing the performance of waveguide filters using additive manufacturing," *Proc. IEEE*, vol. 105, no. 4, pp. 613–619, Apr. 2017.

[22] G. Addamo et al., "Additive manufacturing of Ka-band dual-polarization waveguide components," *IEEE Trans. Microw. Theory Techn.*, vol. 66, no. 8, pp. 3589–3596, Aug. 2018.

[23] A. I. Dimitriadis, M. Favre, M. Billod, J.-P. Ansermet, and E. de Rijk, "Design and fabrication of a lightweight additive-manufactured Ka-band horn antenna array," in *Proc. 10th Eur. Conf. Antennas Propag. (EuCAP)*, Apr. 2016, pp. 1–4.

[24] J. S. Chieh, B. Dick, S. Loui, and J. D. Rockway, "Development of a Ku-band corrugated conical horn using 3-D print technology," *IEEE Antennas Wireless Propag. Lett.*, vol. 13, pp. 201–204, 2014.

[25] J. Tak, D.-G. Kang, and J. Choi, "A lightweight waveguide horn antenna made via 3D printing and conductive spray coating," *Microw. Opt. Technol. Lett.*, vol. 59, no. 3, pp. 727–729, Jan. 2017. [Online]. Available: https://onlinelibrary.wiley.com/doi/abs/10.1002/mop.30374

[26] J. S. Silva, M. García-Vigueras, T. Debogovic, J. R. Costa, C. A. Fernandes, and J. R. Mosig, "Stereolithography-based antennas for satellite communications in Ka-band," *Proc. IEEE*, vol. 105, no. 4, pp. 655–667, Apr. 2017.

[27] D. Henry, A. E. S. Ahmad, A. H. Djilani, P. Pons, and H. Aubert, "Wireless reading of additively manufactured galinstan-based sensor using a polarimetric millimeter-wave radar imaging technique," in *IEEE MTT-S Int. Microw. Symp. Dig.*, Jun. 2023.

[28] M. Knoblauch, J. M. Hibberd, J. C. Gray, and A. J. E. van Bel, "A galinstan expansion femtosyringe for microinjection of eukaryotic organelles and prokaryotes," *Nature Biotechnol.*, vol. 17, no. 9, pp. 906–909, Sep. 1999.

[29] A. Traille et al., "A wireless passive RCS-based temperature sensor using liquid metal and microfluidics technologies," in *Proc. 41st Eur. Microw. Conf.*, Oct. 2011, pp. 45–48.

[30] M. Cosker, F. Ferrero, L. Lizzi, R. Staraj, and J.-M. Ribero, "3D flexible antenna realization process using liquid metal and additive technology," in *Proc. IEEE Int. Symp. Antennas Propag.*, Jun. 2016, pp. 809–810.

[31] V. Bharambe, D. P. Parekh, C. Ladd, K. Moussa, M. D. Dickey, and J. J. Adams, "Vacuum-filling of liquid metals for 3D printed RF antennas," *Additive Manuf.*, vol. 18, pp. 221–227, Dec. 2017. [Online]. Available: https://www.sciencedirect.com/science/article/pii/S2214860417301525

[32] W. Su, S. A. Nauroze, B. Ryan, and M. M. Tentzeris, "Novel 3D printed liquid-metal-alloy microfluidics-based zigzag and helical antennas for origami reconfigurable antenna 'trees,"' in *IEEE MTT-S Int. Microw. Symp. Dig.*, Jun. 2017, pp. 1579–1582.

[33] V. Palazzi, P. Mezzanotte, F. Alimenti, M. Tentzeris, and L. Roselli, "Microfluidics-based 3D-printed 4×4 Butler matrix in coaxial technology for applications up to K band," in *IEEE MTT-S Int. Microw. Symp. Dig.*, Jun. 2019, pp. 1371–1374.

[34] D. Psychogiou and K. Sadasivan, "Tunable coaxial cavity resonator-based filters using actuated liquid metal posts," *IEEE Microw. Wireless Compon. Lett.*, vol. 29, no. 12, pp. 763–766, Dec. 2019.

[35] A. Dyussembayev and D. Psychogiou, "Continuously tunable 3-D printed helical resonators and bandpass filters using actuated liquid metals," *IEEE Microw. Wireless Compon. Lett.*, vol. 32, no. 7, pp. 855–858, Jul. 2022.

[36] J. H. Dang, R. C. Gough, A. M. Morishita, A. T. Ohta, and W. A. Shiroma, "A tunable X-band substrate integrated waveguide cavity filter using reconfigurable liquid-metal perturbing posts," in *IEEE MTT-S Int. Microw. Symp. Dig.*, May 2015, pp. 1–4.

[37] G. Mumcu, A. Dey, and T. Palomo, "Frequency-agile bandpass filters using liquid metal tunable broadside coupled split ring resonators," *IEEE Microw. Wireless Compon. Lett.*, vol. 23, no. 4, pp. 187–189, Apr. 2013.

[38] A. H. Pham, S. Saeedi, and H. H. Sigmarsson, "Continuously-tunable substrate integrated waveguide bandpass filter actuated by liquid metal," in *IEEE MTT-S Int. Microw. Symp. Dig.*, Jun. 2019, pp. 21–23.

[39] X. Liu, L. P. B. Katehi, and D. Peroulis, "Non-toxic liquid metal microstrip resonators," in *Proc. Asia Pacific Microw. Conf.*, Dec. 2009, pp. 131–134.

[40] S. Alkaraki, A. L. Borja, J. R. Kelly, R. Mittra, and Y. Gao, "Reconfigurable liquid metal-based SIW phase shifter," *IEEE Trans. Microw. Theory Techn.*, vol. 70, no. 1, pp. 323–333, Jan. 2022.

[41] M. Li and N. Behdad, "Fluidically tunable frequency selective/phase shifting surfaces for high-power microwave applications," *IEEE Trans. Antennas Propag.*, vol. 60, no. 6, pp. 2748–2759, Jun. 2012.

[42] A. Qaroot and G. Mumcu, "Microfluidically reconfigurable reflection phase shifter," *IEEE Microw. Wireless Compon. Lett.*, vol. 28, no. 8, pp. 684–686, Aug. 2018.

[43] *IMST Radar Small and Flexible Radar Modules by IMST*. Accessed: Sep. 26, 2022. [Online]. Available: http://www.radar-sensor.com/

[44] F. Gao and L. Han, "Implementing the Nelder–Mead simplex algorithm with adaptive parameters," *Comput. Optim. Appl.*, vol. 51, no. 1, pp. 259–277, Jan. 2012.

[45] F. Pedregosa, S. Varoquaux, A. Gramfort, V. Michel, and B. Thirion, "Scikit-learn: Machine learning in Python," *J. Mach. Learn. Res.*, vol. 12, pp. 2825–2830, Dec. 2011.

[46] D. Henry and H. Aubert, "Isolines in 3D radar images for remote sensing applications," in *Proc. 16th Eur. Radar Conf. (EuRAD)*, Oct. 2019, pp. 69–72.

Dominique Henry received the M.S. degree in electronic engineering and the Ph.D. degree from the National Polytechnic Institute, Toulouse, France, in 2012 and 2018, respectively.

From 2013 to 2022, he worked successively as a Research Engineer, a Ph.D. Student, and a Post-Doctoral Researcher with the Laboratory for the Analysis and Architecture of Systems, National Center for Scientific Research (LAAS-CNRS), Toulouse, where he has been a Researcher since 2023. In 2022, he joined the National Research Institute for Agriculture (INRAe), Toulouse, to work on animal radar tracking and detection in farming applications. His research interests include microwave radars, remote sensing, signal processing, and microwave imaging.

Ahmad El Sayed Ahmad was born in Lebanon, in 1984. He received the M.S. degree in high-frequency telecommunications from the University of Limoges, Limoges, France, in 2007, and the Ph.D. degree in telecommunications from the XLIM Research Laboratory, University of Limoges, in 2010.

Then, he held a post-doctoral position at the Institut National des Sciences Appliques (INSA), Rennes, France, until July 2013. From October 2013 to December 2020, he was an Associate Professor with the Faculty of Sciences, Lebanese University, Hadath, Lebanon, and the American University of Lebanon (AUL Arts, Sciences, and Technology University), Beirut, Lebanon; and a Researcher Engineer with the Doctoral School, Lebanese University. From April 2021 to September 2022, he was a Research Engineer with the Laboratory for the Analysis and Architecture of Systems, National Center for Scientific Research (LAAS-CNRS), Toulouse. He has dual citizenship (French and Lebanese). His research interests include mutual coupling effects, broadband and multiband antennas, circularly polarized antennas, printed antennas, yagi antennas, and waveguide antennas.

Ali Hadj Djilani was born in Algeria, in 1995. He received the M.S. degree in signal and image processing for spatial and audio video applications from the University of Paul Sabatier, Toulouse, France, in 2021. He is currently pursuing the Ph.D. degree at the Laboratory for the Analysis and Architecture of Systems, National Center for Scientific Research (LAAS-CNRS), Toulouse, and the National Polytechnic Institute of Toulouse (INPT), Toulouse.

His Ph.D. research focuses on wireless identification and remote reading of passive sensors using millimeter-wave radar imaging techniques.

Patrick Pons was born in Toulouse, France, in May 1963. He received the master's degree in physics, the master's degree in micro-electronics, and the Ph.D. degree in electronics from the University of Toulouse, Toulouse, in 1985, 1986, and 1990, respectively.

Since 1991, he has been a Researcher with the Laboratory of Analysis and Analysis of Systems, National Scientific Research Center (LAAS-CNRS), Toulouse. He is the author or coauthor of more than 95 articles in refereed international journals and more than 267 communications at international conferences. He holds three international patents in the area of micro-sensors and has performed three technological transfers with industrial partners. He was involved in 79 funded projects, including 13 as a coordinator (22 international, 31 national, 12 regional, and 14 industrial). He has been the advisor or co-advisor of 30 Ph.D. students. His research interests are focused on micro-technologies and micro-sensors.

Dr. Pons was a member of the Steering Committee of the "Micro Mechanics Europe" International Conference from 2009 to 2013. He organized the "Eurosensors" International Conference in 1994 and was the Chairperson of the "Micro Mechanics Europe" International Conference in 2009. He was a member of several program committees for international conferences, such as Micromechanics and Micro Systems Europe (MME), IEEE Sensors, Sensornet, and Eurosensors; and is a Reviewer of international journals, such as *Sensors and Actuators*, *Journal of Micromechanics and Microengineering*, *Microelectronic Engineering*, and *Microsystem Technologies*. He has been an Expert at the French Research Agency (ANR) since 2011.

Hervé Aubert was born in Toulouse, France, in July 1966. He received the Eng.Dipl. and Ph.D. (Hons.) degrees in electrical engineering from the National Polytechnic Institute (INPT), Toulouse, in July 1989 and January 1993, respectively.

From April 1997 to March 1998, he was a Visiting Associate Professor at the School of Engineering and Applied Science, University of Pennsylvania, Philadelphia, PA, USA. Since February 2001, he has been a Professor at National Polytechnic Institute. He joined the Laboratory for the Analysis and Architecture of Systems (LAAS), National Center for Scientific Research (CNRS), Toulouse, in February 2006. He has performed research works on integral equation and variational methods applied to electromagnetic wave propagation and scattering. Currently, his research activities involve the electromagnetic modeling of complex (multi-scale) structures, and the design of passive millimeterwave circuits and wireless sensors. He has authored or coauthored one book (in French in 2003); three book chapters [*Fractals: Theory and Applications in Engineering* (Springer, 1999), *New Trends and Concepts in Microwave Theory and Techniques* (Research Signpost, 2003), and *Advances in Sensors, Big Data and Machine Learning in Intelligent Animal Farming* (Multidisciplinary Digital Publishing Institute 2022)]; 102 articles in refereed journals; 219 communications in international symposium proceedings; and 37 invited communications in international conferences, workshops, and convened sessions. He holds nine international patents.

Dr. Aubert serves as a Subject Editor in-Chief since 2020 and Subject Editor (since 2016) of *Electronics Letters*. He served as an Associate Editor for this Journal from 2015 to 2016. He received the European Microwave Association Award in Recognition of Distinguished Service as General Chairperson of the European Microwave Week 2015, the Best Reviewer Award of Information & Communications Technology Express in 2019, the Certificate from IEEE Antennas and Propagation Society in Recognition and Appreciation for Exceptional Performance as a Reviewer of the IEEE TRANSACTIONS ON ANTENNAS AND PROPAGATION in 2021 and 2022.